Inflationary features and shifts in cosmological parameters from Planck 2015 data

Georges Obied, Cora Dvorkin, Chen Heinrich, Wayne Hu, and Vinicius Miranda

Inflationary Features and Shifts in Cosmological Parameters from *Planck* 2015 Data

Georges Obied,[1] Cora Dvorkin,[1] Chen Heinrich,[2] Wayne Hu,[2] and Vinicius Miranda[3]

[1]*Harvard University, Department of Physics,*
Cambridge, MA 02138, USA
[2]*Kavli Institute for Cosmological Physics, Department of Astronomy & Astrophysics,*
Enrico Fermi Institute, University of Chicago, Chicago, IL 60637
[3]*Center for Particle Cosmology, Department of Physics and Astronomy,*
University of Pennsylvania, Philadelphia, Pennsylvania 19104, USA

We explore the relationship between features in the *Planck* 2015 temperature and polarization data, shifts in the cosmological parameters, and features from inflation. Residuals in the temperature data from the best fit power-law ΛCDM model at low multipole $\ell \lesssim 40$ are mainly responsible for the high H_0 and low $\sigma_8 \Omega_m^{1/2}$ values when comparing the $\ell < 1000$ portion to the full dataset. These same residuals are better fit to inflationary features with a 1.9σ preference for running of the running of the tilt or a stronger 99% CL local significance preference for a sharp drop in power around $k = 0.004 \, \mathrm{Mpc}^{-1}$, relieving the internal tension with H_0. At $\ell > 1000$, the same in-phase acoustic residuals that drive the global H_0 constraints and appear as a lensing anomaly also favor running parameters which allow even lower H_0, but not once lensing reconstruction is considered. Polarization spectra are intrinsically highly sensitive to these parameter shifts, and even more so in the *Planck* 2015 TE data due to an anomalous suppression in power at $\ell \approx 165$, which disfavors the best fit H_0 ΛCDM solution by more than 2σ, and high H_0 value at almost 3σ. Current polarization data also slightly enhance the significance of a sharp suppression of large-scale power but leave room for large improvements in the future with cosmic variance limited E-mode measurements.

I. INTRODUCTION

The anisotropies of the cosmic microwave background (CMB) continue to be one of the most powerful probes we have to study physical conditions in the early universe. With the release of *Planck* 2015 data, we now have access to precise all-sky measurements of the polarization as well as the temperature fluctuations of the CMB. Observations from supernovae, baryon acoustic oscillations, Big Bang Nucleosynthesis, among other datasets support, in addition to the CMB, a broadly consistent cosmological model termed ΛCDM.

Nonetheless, evidence for features beyond ΛCDM in the CMB temperature data have been claimed (e.g. [1–9]), as well as disagreements between CMB predictions for local observables under ΛCDM and their measured values (e.g. the local expansion rate H_0 [7, 10]). The two are related because these local cosmological inferences depend on the assumptions in the ΛCDM model, in particular the form of the inflationary power spectrum. It is, thus, essential to consider the impact of one type of deviation from ΛCDM on the other. Moreover polarization data play an essential role in breaking degeneracies between the two. It is the aim of this paper to examine these relationships between features in the temperature and polarization data, shifts in cosmological parameters and inflationary features.

Previous studies have tested the consistency of *Planck* data at different stages in the chain of inference from the raw data to cosmological parameters (e.g. [11–13]). In particular, Ref. [13] split the temperature power spectrum into two disjoint multipole ranges, the lower being similar to the range of WMAP, and analyzed the two ranges separately. They then find a $\sim 2-3\sigma$ discrepancy between parameters (e.g. H_0 and $\Omega_c h^2$) derived from the two parts of the same dataset. The *Planck* collaboration [14] carried out a meticulous investigation of the cause of this tension and discovered that it was mainly due to a deficit in power at low-ℓ and oscillatory residuals in the multipole range $\ell \gtrsim 10^3$. More recently, Ref. [15] examined the consistency of the polarization and temperature datasets, finding no strong evidence to disfavor the ΛCDM model.

In addition, several works [5, 16–26] have explored the effects of inflationary features on CMB observables, including the central role polarization data play in confirming or rejecting such features. For instance, step-like features in the inflationary potential could cause a dip and bump in the temperature data at low ℓ. Such models could arise from symmetry-breaking phase transitions in the early universe, among other reasons [27–30]. These features invariably violate the slow-roll approximation and, thus, require more sophisticated modeling of the resultant inflationary power spectrum. Tension with local measurements of H_0 has also motivated the investigation of new physics at late times [31–54].

In this paper, we adopt both the traditional running of the tilt type parameters and the generalized slow roll (GSR) formalism [23, 55–57], which allows the inclusion of extra 'spline basis' parameters that accommodate order unity power spectrum variations from slow roll predictions. We study the shifts in cosmological parameters, such as H_0 and the amplitude of local structure, when these extra parameters are included and explore the aspects of the temperature and polarization data that drive them.

This paper is organized as follows. Sec. II describes the datasets and parameter inference techniques. The

Dataset	Likelihood
TT	binned TT + low TEB
TTEE	binned TTTEEE + low TEB
$\phi\phi$	lens reconstruction

TABLE I. Combinations of *Planck* 2015 data sets and likelihoods.[a] In addition, we split the binned TT and TTTEEE likelihoods multipole ranges, the latter with a modified likelihood code.

[a] Specifically:
  low TEB = `lowl_SMW_70_dx11d_2014_10_03_v5c_Ap`
  binned TT = `plik_dx11dr2_HM_v18_TT`
  binned TTTEEE = `plik_dx11dr2_HM_v18_TTTEEE`
  lens reconstruction = `smica.g30_ftl_full_pp`, $40 \leq \ell \leq 400$

Model	Parameters $\{\tau, \theta_{MC}, \Omega_b h^2, \Omega_c h^2\}$
ΛCDM	$+\{A_s, n_s\}$
rΛCDM	$+\{A_s, n_s, n_{run}, n_{run,run}\}$
SB	$+\{A_s, n_s, p_i\}$
rSB	$+\{A_s, n_s, n_{run}, n_{run,run}, p_i\}$

TABLE II. Models and parameterizations of the inflationary power spectrum. The parameters p_i are spline basis coefficients that generalize the tilt as defined in Appendix A. In each case, the 4 late time cosmological parameters are prepended to the parameter list.

results of our analyses are presented in Sec. III, which focuses on the shifts in cosmological parameters, and in Sec. IV, which focuses on the implications for inflationary features. We conclude in Sec. V.

II. DATA AND MODELS

For the analyses described in this paper, we use the publicly available *Planck* 2015 data, which include the power spectra of cosmic microwave background (CMB) temperature and polarization fluctuations. For the low multipole ($2 \leq \ell \leq 29$) range, we use the standard `lowTEB` likelihood code supplied by the *Planck* collaboration. For the high multipole ($\ell \geq 30$) range, we similarly use the *Planck* `plik` binned[*1] TT likelihood for the baseline and the TTTEEE likelihood to assess the impact of the polarization data. Note that the low-ℓ polarization data are included in all analyses, even though we refer to these cases as "TT" and "TTEE" respectively. We also alter the ℓ range of the different likelihoods to probe the impact of specific regions of the data, in the case of the TTTEEE likelihood using a custom modification of the code. In some cases, we use information from the *Planck* lensing power spectrum $C_\ell^{\phi\phi}$ in the multipole range $40 \leq \ell \leq 400$. We also include the standard fore-

ground parameters in each analysis.[*2] These datasets and likelihoods are summarized in Tab. I.

We employ a Bayesian approach to infer parameter posterior distributions and to derive confidence limits, namely the Markov Chain Monte Carlo (MCMC) technique implemented via the publicly available `CosmoMC` code [58] linked to a modified version of the Boltzmann code `CAMB` [59]. For each combination of datasets and models, we run 4 MCMC chains until convergence, determined by the Gelman-Rubin criterion $R - 1 < 0.01$.

For the parameters, we take in all cases the standard 4 late-time ΛCDM cosmological parameters: the optical depth to reionization τ, the (approximate) angular scale of the sound horizon θ_{MC}, the baryon density $\Omega_b h^2$ and the cold dark matter density $\Omega_c h^2$. Tensions in the ΛCDM cosmology are mainly associated with $\Omega_c h^2$, which determines the calibration of the physical scale of the sound horizon and, hence, the CMB inference of the Hubble constant H_0 as well as the growth of structure and lensing observables represented by $\sigma_8 \Omega_m^{1/2}$. These two parameters expose tensions in the ΛCDM model when compared to local, non-CMB measurements. Here and throughout the paper, σ_8 is the rms of the linear density field smoothed with a tophat at $8h^{-1}$ Mpc and $\Omega_m = \Omega_c + \Omega_b + \Omega_\nu$. We assume one massive neutrino with $m_\nu = 0.06$ eV and the usual $N_{eff} = 3.046$. We summarize our model and parameter choices in Tab. II.

In Fig. 1 we show the parameter derivatives or responses of the TT, TE and EE power spectra around the best fit ΛCDM model to the TT *Planck* dataset given in Tab. III. Here we normalize the derivatives to σ_ℓ, the cosmic variance per multipole, where

$$\sigma_\ell = \begin{cases} \sqrt{\frac{2}{2\ell+1}} C_\ell^{TT}, & TT; \\ \sqrt{\frac{1}{2\ell+1}} \sqrt{C_\ell^{TT} C_\ell^{EE} + (C_\ell^{TE})^2}, & TE; \\ \sqrt{\frac{2}{2\ell+1}} C_\ell^{EE}, & EE. \end{cases} \quad (1)$$

Here and below σ_ℓ is fixed by the fiducial TT model when varying parameters. For TT and EE this rescaling produces fractional derivatives scaled by $\sim \ell^{-1/2}$ at $\ell \gg 1$, which has the benefit of removing features from parameters like normalization that simply echo the acoustic peaks in the spectrum. We have also rescaled the parameters to either the error in the parameter from the ΛCDM TT model, e.g. for $\Omega_c h^2$ we show the parameter $p = \Omega_c h^2 / \sigma(\Omega_c h^2)$, or by a fixed number, e.g. for n_{run}, $p = 50 n_{run}$ for clarity. For the cases where we scale to σ, this has the added benefit of showing where current limits can be improved with better measurements.

[*1] We have separately tested that the unbinned likelihoods give statistically indistinguishable results.

[*2] Premarginalizing foregrounds assuming ΛCDM with `plik-lite` as in Ref. [14] can change inferences on the inflationary running parameters. Conversely, not using the whole range in ℓ to constrain foregrounds allows $\ell < 1000$ models that do not provide a good global fit to foregrounds (see Tab. III and [14]).
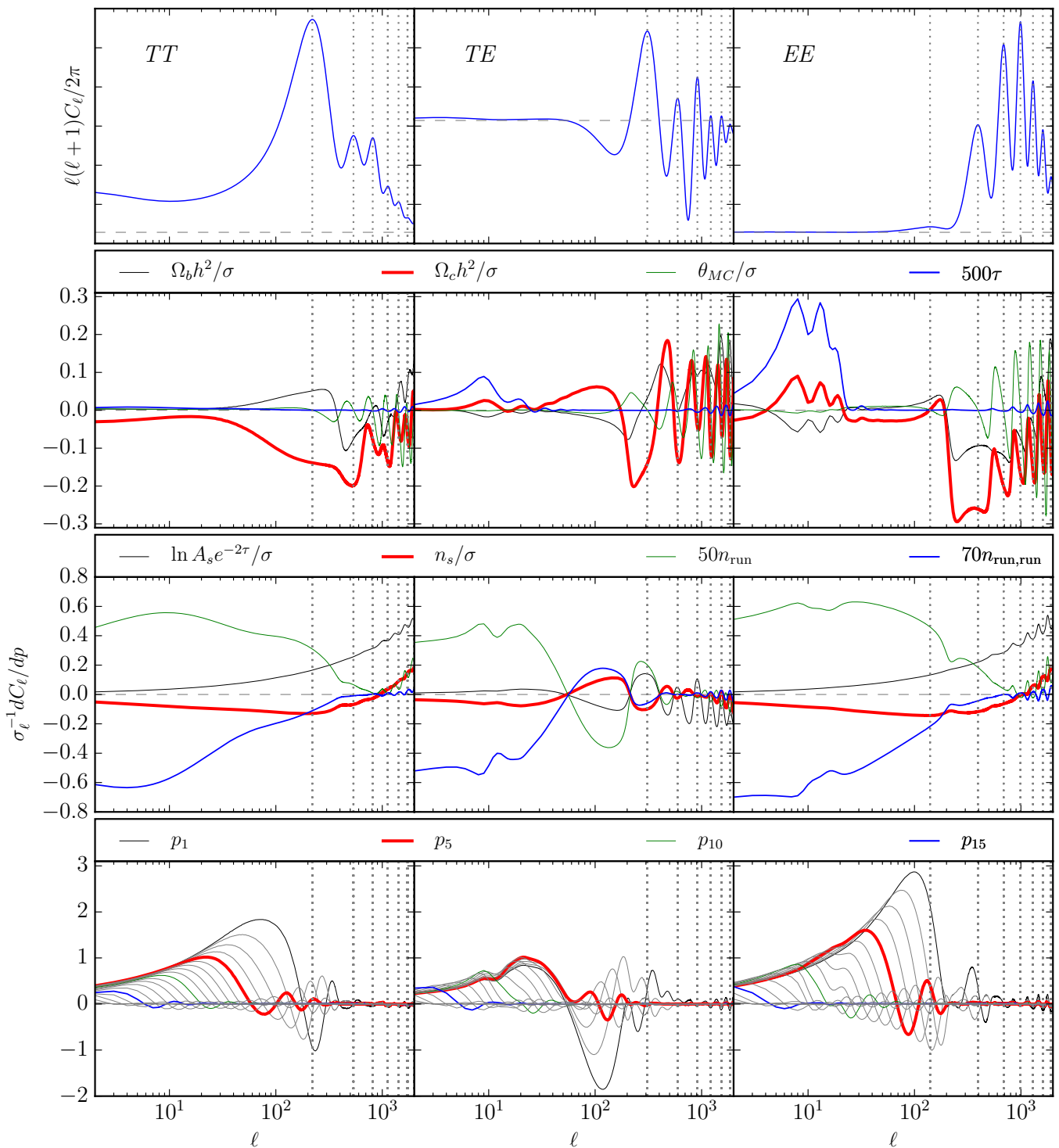
FIG. 1. Response of the TT, TE, EE power spectra to various parameters around the ΛCDM TT model of Tab. III. Derivatives are scaled by σ_ℓ, the cosmic variance error per ℓ of the model, and parameters are scaled by either their *Planck* 2015 ΛCDM TT error σ or by a fixed number for visibility. Vertical dotted lines are drawn at the acoustic peak locations and horizontal dashed lines at zero levels.

Increasing $\Omega_c h^2$ decreases the overall power in the first few acoustic peaks in TT due to the reduction of radiation driving and the early ISW effects from decaying potentials inside the sound horizon (see [60] Fig. 4). Since the former effect changes the amplitude of acoustic os-

cillations, it also reduces the temperature peaks, which are extrema of the oscillations, relative to troughs, which are nodes. Before the damping tail, these changes are nearly in phase with the acoustic peaks in contrast to θ_{MC}, which makes out-of-phase changes that shift peak

Parameter	ΛCDM TT	ΛCDM TT ($\ell < 1000$)	rΛCDM TT	rΛCDM TT$+\phi\phi$	SB TT	rSB TT
$100\Omega_b h^2$	2.22	2.26	2.20	2.20	2.23	2.20
$\Omega_c h^2$	0.120	0.115	0.121	0.120	0.121	0.121
$100\theta_{MC}$	1.0409	1.0408	1.0407	1.0409	1.0409	1.0407
100τ	7.61	7.51	8.66	6.39	9.02	7.96
$\ln(10^{10} A_s)$	3.07	3.06	3.09	3.04	3.10	3.08
n_s	0.965	0.980	0.970	0.972	0.962	0.970
H_0 [km s^{-1} Mpc^{-1}]	67.3	69.4	66.5	67.1	67.0	66.5
$\sigma_8 \Omega_m^{1/2}$	0.465	0.432	0.483	0.463	0.476	0.480

TABLE III. Cosmological parameters of best fit models for various datasets. In the ΛCDM TT ($\ell < 1000$) model the best fit assumes the foreground model of the best fit ΛCDM TT model, unlike the MCMC results where foregrounds are jointly fit. This assures a good global fit when foregrounds are ill-constrained by subsets of the data.

positions. Due to its exponential dependence on the angular scale ℓ, damping tends to shift the observed peak locations to larger angles, the phasing of the two drifts at high ℓ, but we will nonetheless refer to them as "in phase" and "out of phase" oscillatory changes since our focus is on the peaks that are well measured by Planck. Note that with higher multipole information from ground based experiments this effect can be distinguished from entirely in phase effects. Indeed increasing $\Omega_c h^2$ also increases the gravitational lensing, which also reduces the peaks relative to the troughs and remains entirely in phase through the damping tail. For the Planck data, the acoustic effect of $\Omega_c h^2$ is larger than the lensing effect but they both contribute [14].

The impact of $\Omega_c h^2$ on the EE spectrum is much sharper near the sound horizon ($\ell \approx 200$, first polarization trough, see Fig. 3 in Ref. [61] and Ref. [62]) since potential decay does not change it after recombination as it does temperature through the early ISW effect. This enhanced sensitivity carries over to the TE spectrum, which dominates the Planck polarization constraints at high ℓ.

To infer the 4 late-time parameters from CMB data we must assume a parameterized form for the inflationary curvature spectrum $\Delta_{\mathcal{R}}^2$, and vice versa. We choose to model $\Delta_{\mathcal{R}}^2$ in 4 ways to highlight its impact. In all cases, A_s is the amplitude $\Delta_{\mathcal{R}}^2(k_0) = A_s$ where $k_0 = 0.08$ Mpc^{-1}. Fig. 1 shows that this choice places the pivot point at $\ell \approx 10^3$, which is near the best constrained scale of the Planck data. It also shows the effect of raising lensing by raising A_s in the oscillatory response beyond the third peak.

For the slope $d\ln\Delta_{\mathcal{R}}^2/d\ln k$, we consider a constant tilt $n_s - 1$ as the baseline case, which we call "ΛCDM". Unlike the late-time cosmological parameters, A_s and n_s coherently change the TT spectrum across all multipoles rather than introducing localized features in $\Delta C_\ell^{\rm TT}/\sigma_\ell$ (see Fig. 1). On the other hand, the dominant source of tension in the ΛCDM model comes from anomalies in the TT spectrum that are more localized. Fig. 1 shows that by allowing running and "running of the running" of the tilt:

$$\frac{d\ln\Delta_{\mathcal{R}}^2}{d\ln k} = n_s - 1 + n_{\rm run}\ln\left(\frac{k}{k_0}\right) + \frac{n_{\rm run,run}}{2}\ln^2\left(\frac{k}{k_0}\right), \tag{2}$$

one can change the low-multipole part of the spectrum relative to the high-multipole part, but only if these additional parameters are of order the $n_s - 1$ itself. In standard slow roll inflation, each order of running is suppressed by an additional factor of $n_s - 1$, which should make them safely unobservable in the Planck data. We call the case where these parameters are not constrained by the slow roll hierarchy "rΛCDM". In these models, $\Delta_{\mathcal{R}}^2$ will have a prominent but broad feature on CMB scales.

While these parameters can model large-amplitude deviations from slow roll, they cannot model rapid variations that occur on a time scale of an efold or shorter. Such rapid variations would be required to produce sharp features in multipole space in the observed power spectra. To distinguish between rapid variations that are confined to low multipoles and a smooth change in the overall amount of large to small-scale power, we employ the generalized slow-roll (GSR) approximation. Here,

$$\frac{d\ln\Delta_{\mathcal{R}}^2}{d\ln k} \to -G', \tag{3}$$

where G' is a function of efolds of the sound horizon during inflation, as detailed in Appendix A. We consider arbitrary variations $\delta G'$ around both the standard $n_s - 1$ ("SB") and running forms ("rSB") for scales between the horizon and the first acoustic peak. Specifically, we take a spline basis with 20 knots p_i across 2 decades in scale. In Fig. 1 we show the response of the observable power spectrum to these parameters. Note that individually these parameters produce step-like features in the power spectrum and their superposition can produce fine scale features to fit the low-ℓ TT anomalies in the data. In Fig. 1 these steps appear tapered due to rescaling by cosmic variance errors $\sigma_\ell^{-1} \propto \ell^{1/2}$. They produce sharper features in EE at a slightly higher multipole due to projection effects. Since the GSR approximation is still perturbative, we impose an integral constraint on the second
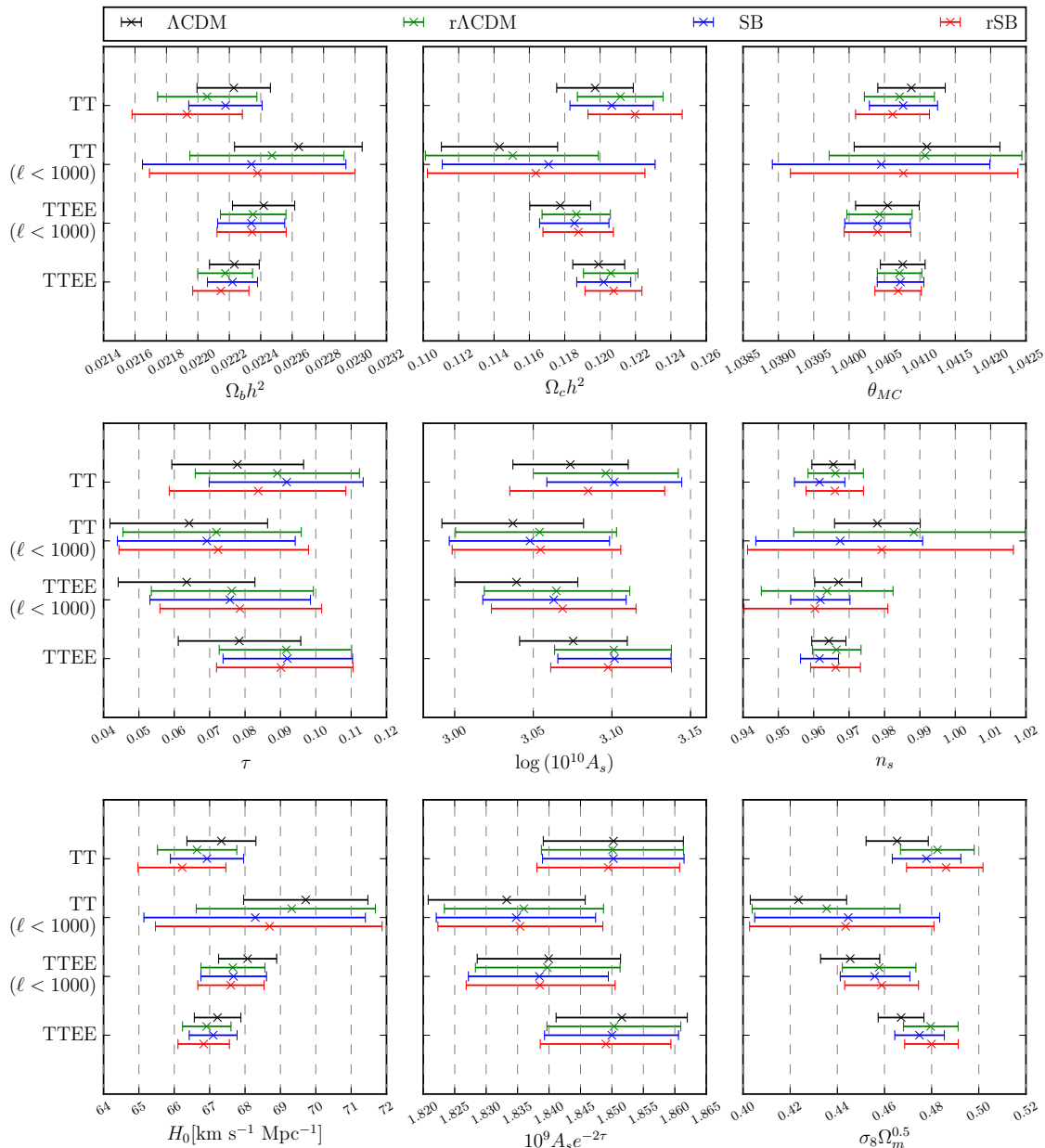
FIG. 2. Cosmological parameter constraints with the 4 combinations of datasets in Tab. I on the 4 models for the inflationary power spectrum in Tab. II.

order impact of the p_i parameters, $\max(I_1) < 1/\sqrt{2}$ (see Eq. A7). Finally, we assume no tensors, $r = 0$ throughout.

Cosmological parameter constraints derived from the MCMC likelihood analyses are summarized in Fig. 2, and best fit models are listed in Tab. III. We use these models in the next two sections to highlight the interplay of features in the data, shifts in cosmological parameters, and features in inflation.

III. H_0 AND COSMOLOGICAL PARAMETERS

Of the 4 late-time parameters, the one most dependent on the dataset and model assumptions of the previous section is the cold dark matter density $\Omega_c h^2$ (see Fig. 2), which directly controls the inferences on H_0 and the monitor for the amplitude of structure today $\sigma_8 \Omega_m^{1/2}$. Raising $\Omega_c h^2$ increases the scale of the sound horizon *relative* to the current horizon because of the reduced effect of radiation on the former. Compensating this effect requires a lower Hubble constant to increase the distance to recombination. In ΛCDM the net effect is to keep $\Omega_m h^3$
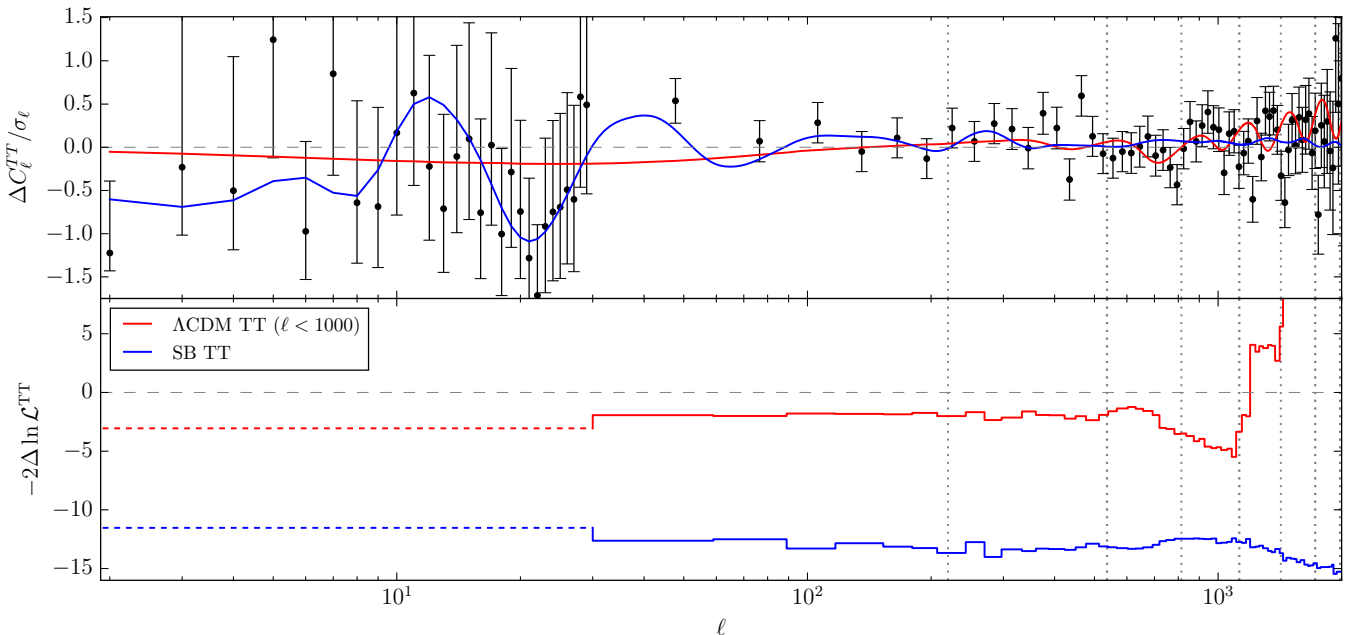
FIG. 3. Top panel: residuals in the TT data (points) and models relative to the best fit ΛCDM TT model of Tab. III (dashed line). Bottom panel: change in the likelihood $2\Delta\ln\mathcal{L}^{\mathrm{TT}}$ of models relative to ΛCDM TT starting from the lowest bin at $2 \leq \ell < 30$ (dotted lines) and adding each individual data point thereafter. The ΛCDM TT ($\ell < 1000$) model (red line) fits the residuals at low $\ell \lesssim 40$ and $\ell \sim 700-1000$ better due to changes in H_0 and other parameters, but it is a poor fit to the in-phase residuals at $\ell > 1000$. Conversely, the inflationary feature SB model (blue) fits the low-ℓ residuals yielding a large $2\Delta\ln\mathcal{L}^{\mathrm{TT}} \sim 12$ improvement at low ℓ, but only small changes at high ℓ. Note that the ΛCDM TT ($\ell < 1000$) model has the same foreground parameters as the ΛCDM TT model, and the data points assume TT foregrounds are fixed to the best fit ΛCDM TT values in Ref. [9].
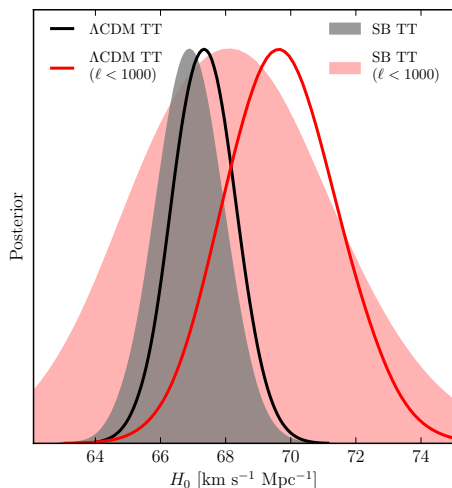

FIG. 4. H_0 from the TT full vs ($\ell < 1000$) datasets. Low-ℓ residuals in Fig. 3 drive H_0 higher in the ΛCDM TT ($\ell < 1000$) analysis (red vs black curves). In the SB model, these residuals are fit by inflationary rather than cosmological parameter changes, so low values of H_0 that are favored in the full analysis (gray shaded) are also compatible in the ($\ell < 1000$, red shaded) analysis.
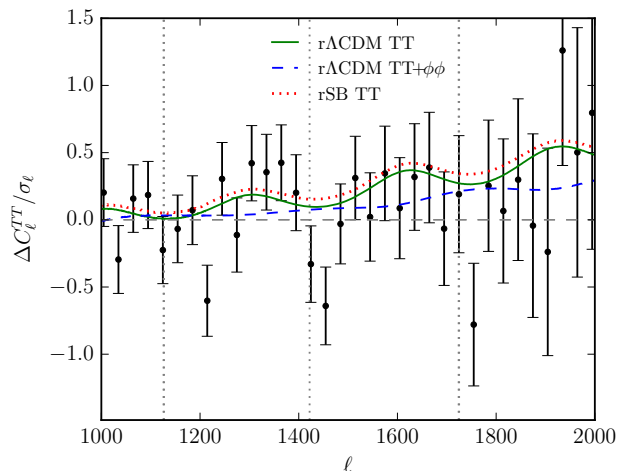

FIG. 5. TT residuals at $\ell > 1000$ relative to the best fit ΛCDM TT model of Tab. III (dashed line). With the running parameters, rΛCDM and rSB seek to fit the oscillatory residuals and make the peaks smoother. Adding the lens reconstruction data $\phi\phi$ largely removes this preference.

nearly constant [63].

As discussed in Ref. [14], this sensitivity is largely driven by the *Planck* TT residuals from the ΛCDM best fit model in two regions: power deficits and glitches at low $\ell \lesssim 40$ and oscillatory residuals at $\ell \gtrsim 10^3$. As shown in Fig. 1, $\Omega_c h^2$ controls the overall amplitude of the acoustic peaks relative to low multipoles, and also impacts the
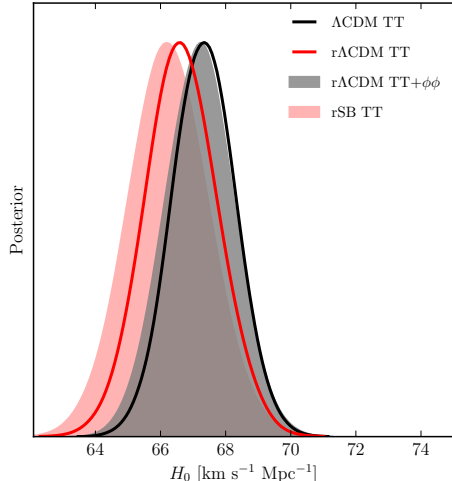
FIG. 6. H_0 and inflationary parameters. In phase $\ell > 1000$ residuals in Fig. 3 drive H_0 lower than the ΛCDM TT model (black) but require running parameters (red curve, rΛCDM; red shaded, rSB) in order to produce a global fit. These fits also predict more gravitational lensing and are not favored by lensing reconstruction data (gray shaded, rΛCDM TT+$\phi\phi$.)

FIG. 7. Lensing power spectrum in the ΛCDM TT model vs. running models rΛCDM TT and rΛCDM TT+$\phi\phi$. Lowering H_0 in the $r\Lambda$CDM model simultaneously raises lensing and is not favored once the lensing reconstruction data (points) are taken into account.

height of the peaks relative to the troughs. Given the ability of the inflationary power spectrum to change the relative power and amount of smoothing of the peaks due to lensing, the interpretation of these residuals depends on the inflationary model assumptions. In addition, as shown in Ref. [9], the TE data have a surprisingly large impact on $\Omega_c h^2$ and H_0, favoring a low value for the latter. We further explore these issues and their relationship to inflationary features in turn.

A. Low $\ell \lesssim 40$ TT residuals

We begin by repeating the test discussed in Ref. [13] of comparing the inferences from the TT and TT ($\ell < 1000$) datasets on H_0 in the ΛCDM model context. In Fig. 4, we show that constraints shift from $H_0 = [67.3 \pm 0.98]$ km s^{-1}Mpc^{-1} to $[69.7 \pm 1.8]$ km s^{-1}Mpc^{-1} , as expected. In Ref. [14], this shift is largely attributed to the low-ℓ residuals between the data and the best fit ΛCDM model to the full-TT data, which we display in Fig. 3.[*3] These residuals favor lower low-ℓ power compared with the acoustic peaks. As seen in Fig. 3 (red curve), they can be fit better by the ΛCDM TT ($\ell < 1000$) model by lowering $\Omega_c h^2$, which increases the radiation driving to raise the peaks over lower ℓ's with adjustments of other pa-
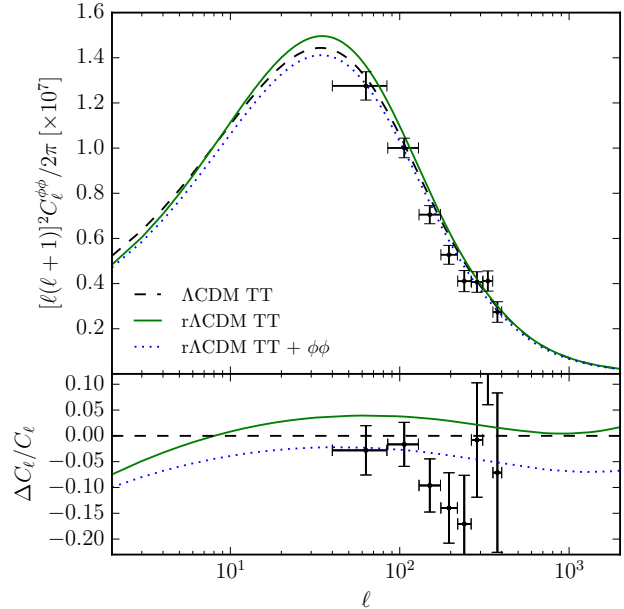
rameters, such as n_s (see Tab. III). In addition, the out-of-phase residuals peaking between the third and fourth acoustic peaks $\ell \approx 700 - 1100$ drive a small change in $\theta_{\rm MC}$. With the full range in TT, these same changes cannot fit the data, as we discuss further in the next section.

To further test this interpretation, we show the impact of generalizing the model class to SB which allows the low-ℓ residuals to be fit by inflationary features instead. The maximum likelihood SB TT model of Tab. III is shown in Fig. 3 (blue curve). By design, the SB parameters do not significantly alter the acoustic peaks (see Fig. 1) leaving the high-ℓ residuals and cosmological parameters nearly unchanged from ΛCDM TT. Correspondingly, in Fig. 4 we show that for the full-TT data set, H_0 constraints also remain largely unchanged, whereas for $\ell < 1000$ they broaden, making these lower H_0 values compatible. From Fig. 2, there is a similar broadening in the running classes of models rΛCDM and rSB. We return to the distinctions between these various means of fitting TT residuals at low ℓ in Section IV (see also Fig. 12).

B. High $\ell \gtrsim 1000$ TT residuals

In the full TT dataset, the lower $\Omega_c h^2$ and higher H_0 that is preferred by the low-ℓ residuals causes even more significant in-phase high-ℓ deviations from the data.

[*3] These data points have a fixed best fit TT foreground model under ΛCDM subtracted. In order to compare the ΛCDM TT ($\ell < 1000$) model to the residuals, we take the best fit with the TT foreground model fixed by the full ℓ range in Tab. III.

Higher radiation driving beyond the 4th peak implies sharper peaks than those seen in the data (see Fig. 5). Indeed, there remains in-phase oscillatory residuals of opposite sign at high $\ell > 1000$ even with respect to the full ΛCDM TT maximum likelihood model. The data favor smoother peaks than those that can be achieved in the ΛCDM context, producing the so-called lensing anomaly, since additional lensing acts to smooth the peaks (see Fig. 1).

Specifically, when allowing the amplitude of lensing $C_\ell^{\phi\phi} \to A_L C_\ell^{\phi\phi}$ to float independently, $A_L = 1.22 \pm 0.10$ [9]. Alternately, if only $\ell > 1000$ data are considered in the ΛCDM context, $H_0 = [64.1 \pm 1.7]$ km s^{-1}Mpc^{-1} as pointed out by Ref. [13]. However, given an inflationary power spectrum described by A_s and n_s as in ΛCDM, fitting the oscillatory residual in this way does not lead to a consistent global solution [14].

Relaxing the assumptions on the inflationary power spectrum allows for greater flexibility. In Fig. 5, we see that moving to the $r\Lambda$CDM and rSB classes does indeed fit the oscillatory residuals better. Correspondingly, in Fig. 6, these classes allow even lower values of $H_0 = 66.6 \pm 1.1$ and 66.2 ± 1.2 km s^{-1}Mpc^{-1} respectively, corresponding to the higher values of $\Omega_c h^2$, as shown in Fig. 2. Note also that this enhanced freedom is also associated with a higher value of τ and, hence, A_s. Given the suppressed curvature power spectrum on large scales, it takes a larger τ to provide the same amplitude of polarization from reionization.

In Fig. 7, we show that the combination of A_s and $\Omega_c h^2$ changes in the $r\Lambda$CDM model from Tab. III also enhances the lensing power spectrum. However, lensing reconstruction data do not favor such an enhancement. In Fig. 6 we see that, correspondingly, the preference for shifting H_0 even lower in the rΛCDM model mainly goes away with the TT+$\phi\phi$ dataset, where $H_0 = 67.2 \pm 1.1$ km s^{-1}Mpc^{-1} .

C. Intermediate $\ell \sim 200$ TE residuals

Ref. [9] showed that the TE data alone constrain H_0 to comparable precision as the full TT data, and that it favors the low H_0 of the latter as opposed to the high H_0 of TT ($\ell < 1000$). We can attribute some of this ability to the enhanced, degeneracy breaking, sensitivity to $\Omega_c h^2$ in the TE and EE spectra around the first polarization trough at $\ell \sim 200$ (see Fig. 1). Given *Planck* noise, TE is more constraining than EE, and so we focus on its impact.

In Fig. 8, we show the TTEE data set inferences on H_0 from the full range and compare it to the $\ell < 1000$ range. Most of the extra information from polarization comes from $\ell < 1000$, as expected given *Planck* noise. While discarding the $\ell > 1000$ range in the TT analysis doubles the H_0 errors, the impact on the TTEE analysis is notably smaller: $H_0 = 68.1 \pm 0.83$ km s^{-1}Mpc^{-1} compared with 67.2 ± 0.66 km s^{-1}Mpc^{-1} Moreover, the TE
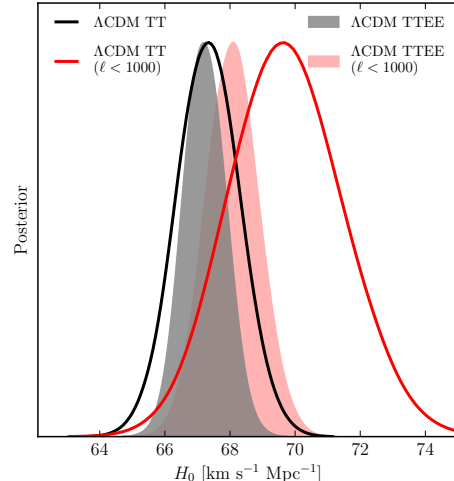

FIG. 8. H_0 and polarization data. TE residuals shown in Fig. 9, especially near $\ell \sim 200$, drive H_0 lower, even in the $\ell < 1000$ datasets (red curves to red shaded), whereas the full data range provide values consistent with ΛCDM TT, with smaller errors.

data at $\ell < 1000$ pulls H_0 closer to the value preferred by the TT dataset of the full rather than $\ell < 1000$ range. On the face of it, this provides independent support for low H_0 that does not involve the multipole ranges known to have anomalies in TT and provides some proof against instrumental systematics. However, even given the large and sharp polarization responses to $\Omega_c h^2$ in Fig. 1, the noisy TE *Planck* data seem unusually sensitive to $\Omega_c h^2$ and H_0.

To better understand the sensitivity, in Fig. 9 we show the residuals of the TE data relative to the best fit ΛCDM TT model and also compare them to the best fit ΛCDM TT ($\ell < 1000$) model. Note that neither cosmological model is optimized to fit the polarization data. Polarized and unpolarized foregrounds are jointly reoptimized in the ΛCDM and SB TT cases, whereas for ΛCDM TT ($\ell < 1000$) they are held fixed to their reoptimized ΛCDM values. The difference between the two models is relatively small compared with the measured errors. However, the data show a significant deviation in the $\ell \sim 165$ bin relative to both models at $\sim 2\sigma$ for the full ΛCDM TT model (low H_0) and $\sim 3\sigma$ for the ΛCDM TT ($\ell < 1000$; high H_0) model. We therefore attribute the enhanced sensitivity to H_0 in large part to the presence of this one outlier.

To test this attribution, we also show in Fig. 9 (bottom panel) the change in the TTEE likelihood between the ΛCDM TT and ΛCDM TT ($\ell < 1000$) models as a function of the maximum ℓ. The ΛCDM TT ($\ell < 1000$) model jumps from a better fit to a worse fit across the $\ell = 165$ bin, unlike with the TT likelihood (cf. Fig. 3). We also show the best fit SB TT model in Fig. 9. Intriguingly, even though this model is not optimized to fit the anomalous low power around $\ell = 165$, it does marginally
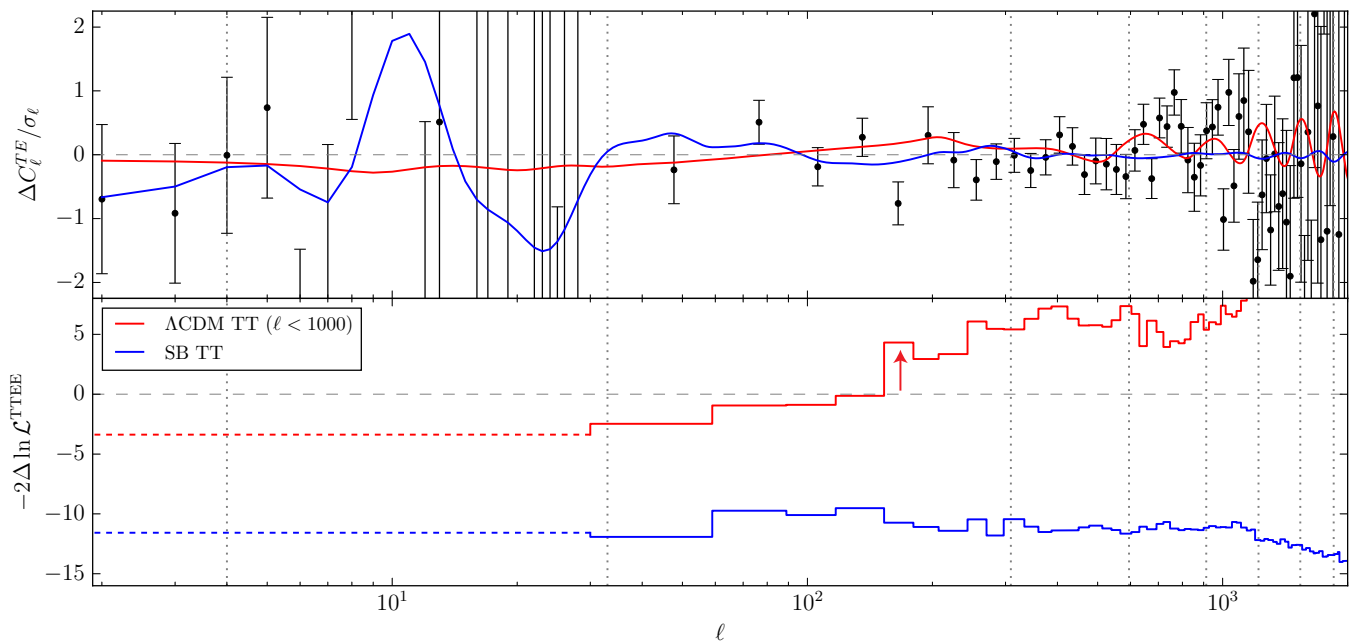
FIG. 9. Top panel: residuals in the TE data (points) and the same models as in Fig. 3 relative to the best fit ΛCDM TT model of Tab. III (dashed line). Bottom panel: $2\Delta \ln \mathcal{L}^{\mathrm{TTEE}}$ of models relative to ΛCDM TT in the same form as Fig. 3. Cosmological parameters are fixed to their TT best fit values and the TT ($\ell < 1000$) model also has the same foreground parameters as the TT model including polarized foregrounds. The ΛCDM TT ($\ell < 1000$) model becomes a worse fit to the TTEE dataset when passing the point at $\ell \approx 165$ (arrow), whereas the SB TT model slightly improves the fit.

reduce tension with that bin. It is also interesting to note that even in the rΛCDM where $H_0 = 66.9 \pm 0.69$ km s^{-1}Mpc^{-1} and rSB classes where $H_0 = 66.8 \pm 0.72$ km s^{-1}Mpc^{-1} , the TTEE data set no longer allows the even lower H_0 values found from fitting the $\ell > 1000$ oscillatory TT residuals even with no lensing reconstruction data (see Fig. 2).

However, the *Planck* collaboration considers the TE and EE data sets as preliminary and so the anomalous sensitivity to H_0 in the ΛCDM context, while intriguing, should not be overinterpreted.

D.   Local amplitude $\sigma_8 \Omega_m^{1/2}$

The lowering of H_0 and raising of Ω_m between the WMAP9 or *Planck* TT ($\ell < 1000$) cosmology and the *Planck* (full) TT cosmology causes an increase in the parameter that monitors local structure $\sigma_8 \Omega_m^{1/2}$ (see Fig. 10). This increase is in moderate tension with measurements of the local cluster abundance, depending on the mass calibration employed [9, 64], and of weak gravitational lensing [65–67].

In Fig. 10, we show the effect of generalizing the model class to rΛCDM. The allowed further raising of $\Omega_c h^2$ and lowering of H_0 with just the TT data set shifts $\sigma_8 \Omega_m^{1/2}$ to higher values. However, once the $\phi\phi$ lensing reconstruction data are included, this preference disappears.
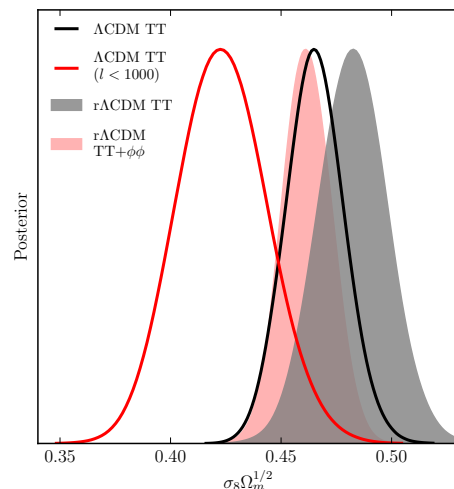

FIG. 10. Amplitude of structure $\sigma_8 \Omega_m^{1/2}$. Shifts in $\Omega_c h^2$ from ΛCDM TT ($\ell < 1000$; red curve) to the full range (black curve) drive $\sigma_8 \Omega_m^{1/2}$ higher. Fitting the in-phase high-ℓ residuals with the enhanced freedom of the rΛCDM model drives it even higher (gray shaded), but in a manner inconsistent with the lensing reconstruction data (red shaded).

IV.   INFLATIONARY FEATURES

The same residuals in the *Planck* TT data that drive shifts in H_0 and $\sigma_8 \Omega_m^{1/2}$ provide hints that inflation
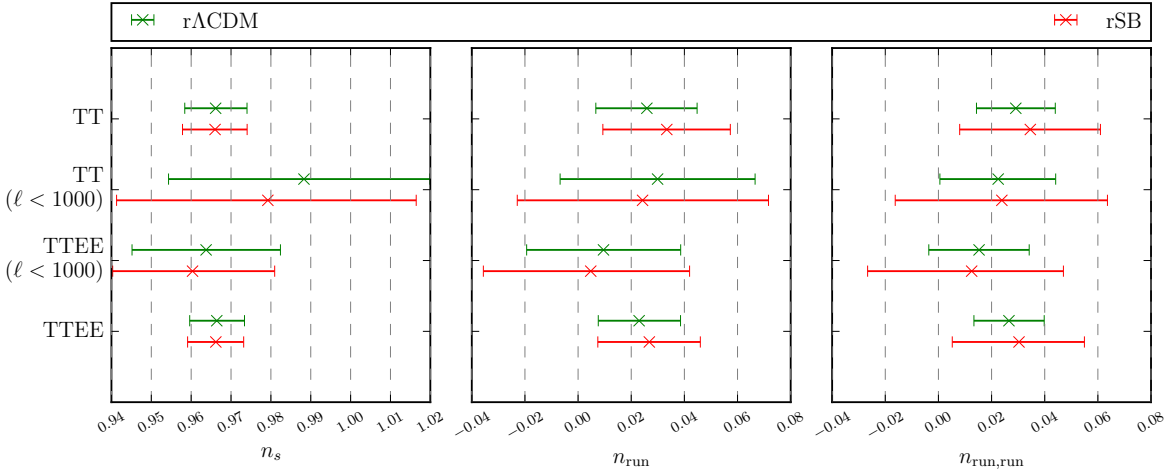
FIG. 11. Constraints on inflationary parameters – tilt, its running, and the running of the running from Eq. 2 – for the 4 combinations of datasets in Tab. I.
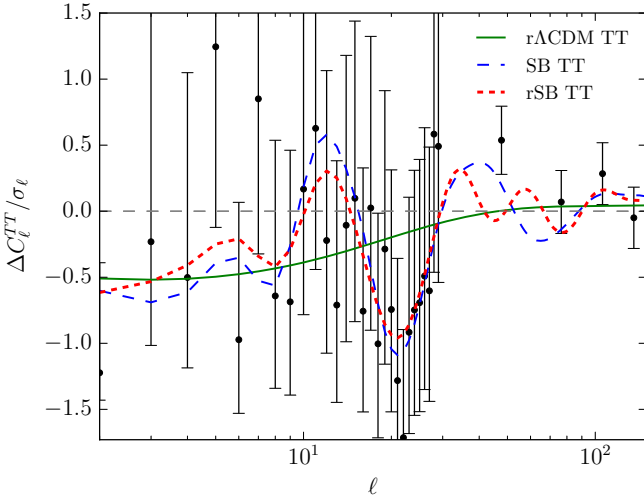

FIG. 12. Low-ℓ TT residuals (points) and models relative to the best fit ΛCDM TT model of Tab. III (black dashed). While the running model rΛCDM TT (green solid) can suppress power, the SB TT model (blue dashed) accommodates the sharp dip favored by the data. Allowing both running and SB in the rSB TT model (red dotted) leads to a similar fit as SB TT.
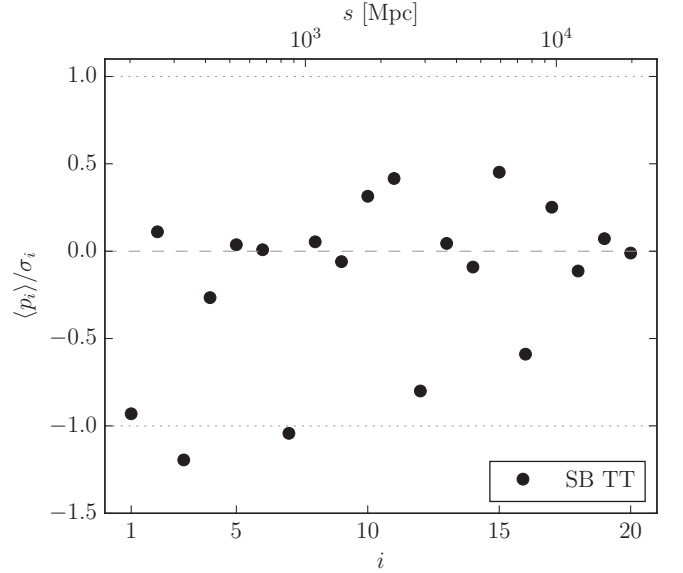

FIG. 13. SB parameters of the SB TT analysis in units of their errors. No single SB parameter p_i is significantly detected due to covariances hidden in the marginalized errors.

Parameter	rΛCDM TT	rΛCDM TT + $\phi\phi$	SB TT	rSB TT
n_{run}	0.033	0.030	—	0.042
$n_{\mathrm{run,run}}$	0.032	0.026	—	0.041
m_1	—	—	0.078	0.025
m_2	—	—	-0.34	-0.085
m_3	—	—	-0.35	-0.12

TABLE IV. Inflationary parameters of best fit models for various datasets. The running parameters are defined in Eq. 2 and m_1, m_2, m_3 are are the first 3 principal components of the SB parameters rank ordered by increasing variance.

may be more complex than single-field slow-roll inflation would imply. No single set of ΛCDM parameters with a power-law curvature power spectrum simultaneously gives a very good fit to the TT data at low ℓ and high ℓ, as shown in Fig. 3.

Although single-field inflation allows for running of the tilt and running of the running, under the slow-roll approximation each order should be successively suppressed by $\mathcal{O}(n_s - 1)$ if there is no special cancellations between slow roll parameters, i.e. $n_{\mathrm{run,run}} \lesssim 10^{-4}$. However, in the r$\Lambda$CDM analysis $n_{\mathrm{run,run}} = 0.029 \pm 0.015$ [9], a 1.9σ preference for a violation of slow-roll inflation (see Fig. 11). In Tab. IV, we give the best fit values for
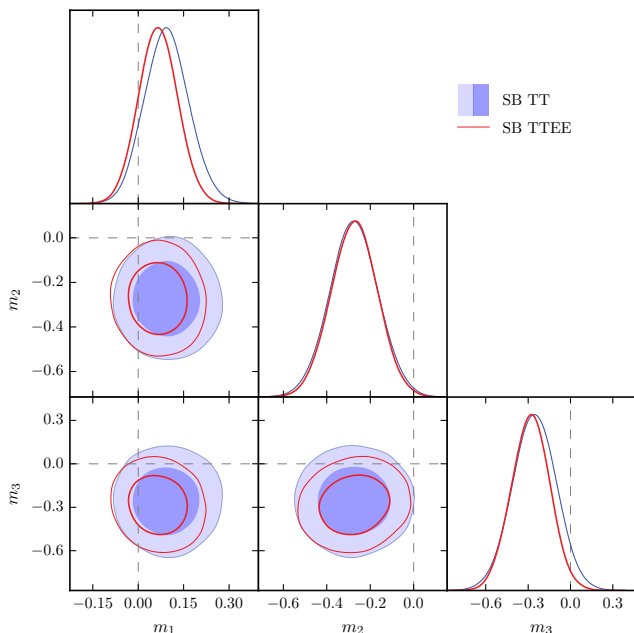
FIG. 14. First 3 principal components of the SB TT p_i covariance matrix in the TT (thin blue) and TTEE (thick red) analysis (68%, 95% CL). Both m_2 and m_3 show non-zero deviations whose significance is slightly enhanced by the addition of polarization information.
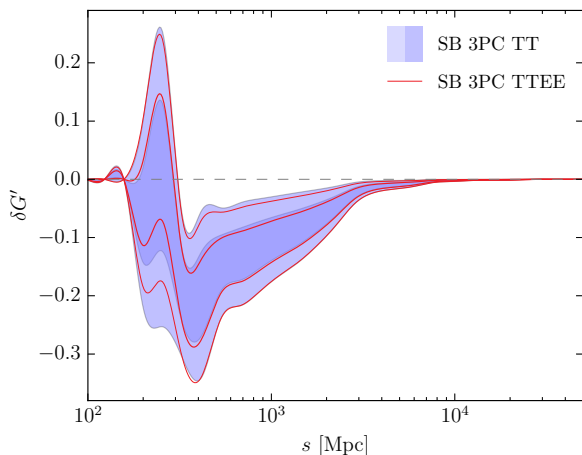

FIG. 15. Functional reconstruction of generalized tilt ($\delta G'$: 68%, 95% CL) from the first 3 principal components in the SB TT (shaded) and SB TTEE (dashed and dotted lines) analyses. Polarization information slightly sharpens the dip near 400 Mpc.

FIG. 16. Functional reconstruction of inflationary power spectrum ($\Delta_{\mathcal{R}}^2$: 68%, 95% CL) from the first 3 principal components in the SB TT (shaded) analysis compared with the best fit running model rΛCDM TT.

running parameters in the various model classes, and in Fig. 12 we show how well these models fit the data residuals at low ℓ. While the rΛCDM model does indeed lower power on large scales, it fails to fit the sharp decline in power at $\ell \sim 20-30$. As shown in Fig. 5, there is also a slight preference for nonzero running parameters due to their ability to accommodate cosmological parameter changes that fit the high-ℓ oscillatory residuals. However, this preference does not remain if the lens reconstruction
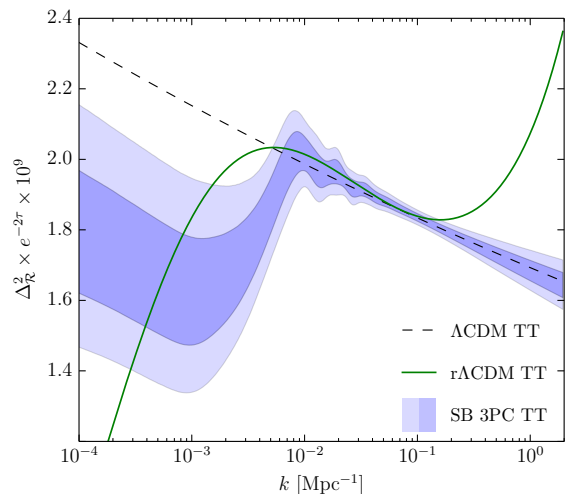
data are considered.

Given the large preferred values of $n_{\rm run,run}$, such models violate slow roll and may in their own right be considered inflationary features, so there is no theoretical motivation to model the inflationary curvature power spectrum as a truncated Taylor expansion around the pivot point as in Eq. (2). Indeed, we see in Fig. 12 that the SB parameters of the generalized tilt $\delta G'$ allow a sharper decline at $\ell \sim 20-30$, which better fits the data. On the other hand, with 20 free parameters, the SB model tends to overfit the residuals leaving highly correlated parameter errors and no single p_i with more than a $\sim 1\sigma$ deviation from the slow roll prediction of zero (see Fig. 13).

From Fig. 3, we see that the net improvement in fitting the residuals with SB at $\ell < 30$ is $2\Delta \ln \mathcal{L}^{\rm TT} \sim 12$. We also show that combining both SB and running parameters leads to fits that are very similar to SB at low ℓ. Correspondingly, once the SB parameters are marginalized, the significance of the preference for finite values decreases to $n_{\rm run,run} = 0.035 \pm 0.027$ (see Fig. 11). Its best fit value 0.041 actually increases in rSB, in part due to its ability to fit the high-ℓ in-phase residuals.

In order to expose the most significant linear combination of the SB p_i parameters and their implications, we examine the m_a principal components (PCs) of its covariance matrix $C_{ij} = \langle p_i p_j \rangle$, rank ordered by increasing eigenvalue or variance, following Ref. [25], as detailed in the Appendix. For the SB TT analysis, the best constrained PCs also contain the most significant deviations from slow roll. Note that $m_2 = m_3 = 0$ is outside the 95% CL region and is in fact excluded at $\sim 99\%$ CL in Fig. 14 with $m_2 = -0.27 \pm 0.11$ and $m_3 = -0.25 \pm 0.16$. Of course one should interpret this as a local significance given the number of well measured PCs that this anomaly could have appeared in. Furthermore, using the SB TT PC basis, we can assess whether the additional polar-

ization information in the TTEE data set supports or weakens this preference. In Fig. 14 we see that polarization enhances the significance of the deviation to 2σ in $m_3 = -0.28 \pm 0.14$ while leaving $m_2 = -0.27 \pm 0.11$ essentially unchanged at $\sim 2.5\sigma$ and improving the bounds on m_1.

Retaining (or "filtering") the SB to only the first 3 PCs ("SB 3PC TT", see Eq. A17), we can better isolate the most significant implications for inflation and the curvature power spectrum. In Fig. 15, we show the inflationary implications for $\delta G'$, the analog of the tilt for models with rapid deviations from slow roll. The 3PC preference is for a $> 95\%$ CL sharp suppression in $\delta G'$ beginning at ~ 300 Mpc and preceded by a less significant enhancement. While the additional polarization information in TTEE does not further enhance the amplitude or significance of the suppression, it does enhance the sharpness.

Finally, in Fig. 16 we show the implications for the curvature power spectrum. Unlike the smooth deviations of the rΛCDM TT model, the SB 3PC TT model has a sharp suppression around $k \approx 0.004$ Mpc^{-1}. In canonical single-field inflation, such a suppression would be associated with an abrupt transition from a faster to a slower rolling rate.

V. DISCUSSION

We have explored the interplay between features from inflation, features in the *Planck* 2015 data, and shifts in the cosmological parameters.

Preference for high H_0 values in ΛCDM from the TT data at $\ell < 1000$ is driven by low $\ell < 40$ residuals in the data, which then prefer the acoustic peaks to be raised by enhancing radiation driving through lowering $\Omega_c h^2$, and consequently raising H_0 to match the angular position of the peaks. However, these cosmological parameter variations do not match the residuals particularly well. If we marginalize their impact on H_0 by fitting, instead, to inflationary features of the generalized tilt $\delta G'$ form in the SB analysis, then the low H_0 favored by the full TT data is compatible with even the $\ell < 1000$ TT data.

Correspondingly, the SB parameters show 2 principal components that jointly deviate from zero at the $\sim 99\%$ CL in local significance. These deviations in $\delta G'$ prefer a sharp suppression of power around $k \approx 0.004$ Mpc^{-1}. The residuals can also be fit to a running of the running of the tilt in the rΛCDM model, but those fits cannot reproduce the sharpness of the suppression. Furthermore, the large running of the running favored would itself represent an inflationary feature in the power spectrum that cannot be explained in slow-roll inflation.

The same $\ell > 1000$ oscillatory TT residuals which drive H_0 lower and $\sigma_8 \Omega_m^{1/2}$ higher in the full TT data set prefer an even lower H_0 if only $\ell > 1000$ is considered [13], but this does not provide a good global fit in ΛCDM with power-law initial conditions [14]. With running parameters in the tilt, $H_0 = 66.6 \pm 1.1$ km s^{-1}Mpc^{-1} . The combination of low-ℓ and high-ℓ anomalies makes running of the running preferred at the 1.9σ level in the TT data set. However, on the low ℓ side, once the sharp feature is marginalized with SB this preference drops to the 1.3σ level. On the high ℓ side, once lensing reconstruction is taken into account, preference for fitting oscillatory residuals disappears and $H_0 = 67.9 \pm 0.92$ km s^{-1}Mpc^{-1} returns to nearly the ΛCDM value.

In polarization, the signature of changes in H_0 through $\Omega_c h^2$ is much sharper and somewhat larger. Polarization suffers less projection effects and lacks the early ISW that broadens the signature in temperature and its measurement at $\ell \sim 200$ is important for assuring the robustness of H_0 inferences from the CMB in ΛCDM.

Indeed, despite being noisier than TT, *Planck* TE data alone already constrain H_0 as well as TT [9]. They also are consistent with the low H_0 constraints from the full TT data, even though their impact comes from $\ell < 1000$. On the other hand, the *Planck* TE data are anomalously sensitive to H_0 due to a deviation in the bin at $\ell \sim 165$, which even more strongly disfavors the high H_0 of the $\ell < 1000$ TT data fit.

Polarization data are also beginning to help constraints on the inflationary features favored by the low-ℓ TT residuals. In *Planck* 2015, only the $\ell \geq 30$ HFI data was released, and so the main effect is to strengthen the confinement of the features to large scales, thus favoring a sharper feature in the joint analysis. This sharpening in turn enhances the significance of the deviations in one of the principal components to 2σ leaving the other at 2.5σ. At $\ell < 30$, only LFI polarization data was released, and the impact of inflationary features is to change inferences on the optical depth τ, since with smaller inflationary power a higher τ is required to produce the same polarization power. In the final *Planck* release, the inclusion of HFI polarization data at $\ell < 30$ should also provide insight on the low-ℓ TT residuals and their implications for inflationary features. It will be important then to distinguish inflationary features from reionization features beyond the simple near instantaneous reionization models used here [68]. We leave these considerations to a future work.

Appendix A: GSR Spline Basis

The GSR approach [55] is a generalization of the slow-roll approximation that allows for features in the power spectrum of $\Delta \ln k \lesssim 1$ in a general single-field model that includes canonical [56], $P(X, \phi)$ [69], and Horndeski (Galileon) inflation [70]. In this approximation, the curvature power spectrum $\Delta_{\mathcal{R}}^2$ is sourced by a single function $f = 2\pi z \sqrt{c_s} s$, where z is the Mukhanov variable in the Mukhanov-Sasaki equation, c_s is the sound speed and s is the sound horizon:

$$ s = \int_a^{a_{\mathrm{end}}} \frac{da}{a} \frac{c_s}{aH}. \tag{A1} $$

Here a_{end} is the scale factor at the end of inflation and H is the Hubble parameter during inflation. For a canonical scalar field in Planck units ϕ, $z = a^2 d\phi/da$.

In the ordinary slow-roll approximation, $\Delta_{\mathcal{R}}^2 \approx f^{-2}$, whereas in GSR:

$$ \ln \Delta_{\mathcal{R}}^2(k) \approx G(\ln s_*) + \int_{s_*}^{\infty} \frac{ds}{s} W(ks) G'(\ln s) \tag{A2} $$
$$ + \ln \left[1 + I_1^2(k)\right], $$

where

$$ G(\ln s) = -2 \ln f + \frac{2}{3}(\ln f)', \tag{A3} $$

with $' = d/d\ln s$ and s_* is an arbitrary epoch during inflation such that all relevant k-modes are well outside the sound horizon, $ks_* \ll 1$. The window functions,

$$ W(x) = \frac{3\sin(2x)}{2x^3} - \frac{3\cos(2x)}{x^2} - \frac{3\sin(2x)}{2x}, \tag{A4} $$

at leading order and

$$ X(x) = \frac{3}{x^3}(\sin x - x \cos x)^2, \tag{A5} $$

at second order through

$$ I_1(k) = \frac{1}{\sqrt{2}} \int_0^{\infty} \frac{ds}{s} G'(\ln s) X(ks), \tag{A6} $$

characterize the freezeout of the source function around sound horizon crossing. This form for the power spectrum remains a good approximation if the second order term [23]

$$ I_1 < \frac{1}{\sqrt{2}}, \tag{A7} $$

and hence allows for up to order unity features in the curvature power spectrum.

The ordinary slow-roll approximation corresponds to $G'(\ln s) = 1 - n_s$, and results in a power-law curvature power spectrum. In the main text, we use GSR to fit the low-ℓ anomalies in the power spectrum, and so we choose to restrict our parameterization of fluctuations, $\delta G'$, around this constant to

$$ 200 < \frac{s}{\mathrm{Mpc}} < 20000. \tag{A8} $$

Next, we follow Ref. [23] in defining a band limit for the frequency of deviations by sampling $p_i = \delta G'(\ln s_i)$ at a rate of 10 per decade for a total of 20 parameters. This rate is sufficient to capture the low-ℓ anomalies. We then construct the smooth function using the natural spline of these points.

Specifically, we exploit the linearity of splines to define the spline basis (SB) functions $B_i(\ln s)$ from the natural spline of the set of unit amplitude perturbations $p_i = 1$, $p_{j \neq i} = 0$. In the SB class of models we then describe the source function as:

$$ G'(\ln s) = (1 - n_s) + \sum_i p_i B_i(\ln s). \tag{A9} $$

The advantage of the GSR form in Eq. (A2) is that the integrals are linear in G' and, hence, the impact of the individual components can be precomputed separately as:

$$ W_i(k) = \int_{s_*}^{\infty} \frac{ds}{s} W(ks) B_i(\ln s), $$
$$ X_i(k) = \int_0^{\infty} \frac{ds}{s} X(ks) B_i(\ln s), \tag{A10} $$

so that the power spectrum becomes a sum over the basis

$$ \ln \Delta_{\mathcal{R}}^2(k) = \ln A_s \left(\frac{k}{k_0}\right)^{n_s - 1} + \sum_i p_i \left[W_i(k) - W_i(k_0)\right] $$
$$ + \ln \left[\frac{1 + I_1^2(k)}{1 + I_1^2(k_0)}\right], \tag{A11} $$

where

$$ I_1(k) = \frac{\pi}{2\sqrt{2}}(1 - n_s) + \frac{1}{\sqrt{2}} \sum_i p_i X_i(k). \tag{A12} $$

Note that we have absorbed the normalization constant $G(\ln s_*)$ into the amplitude of the power spectrum at the scale k_0:

$$ A_s = \Delta_{\mathcal{R}}^2(k_0). \tag{A13} $$

In the rSB class of models we replace the first term in Eq. (A11) with the running form defined by Eq. (2).

Since our choice of parameters oversamples $\delta G'$ relative to what the data can constrain, individual measurements of p_i from the MCMC mainly fit noise with any true signal buried in the covariance between parameters. We therefore construct the principal components derived from an eigenvalue decomposition of the MCMC covariance matrix estimate:

$$ C_{ij} = \langle p_i p_j \rangle - \langle p_i \rangle \langle p_j \rangle $$
$$ = \sum_a S_{ia} \sigma_a^2 S_{ja}, \tag{A14} $$

where S_{ia} is an orthonormal matrix of eigenvectors. Specifically, we define the PC parameters

$$m_a = \sum_i S_{ia} p_i, \qquad (A15)$$

such that their covariance matrix satisfies:

$$\langle m_a m_b \rangle - \langle m_a \rangle \langle m_b \rangle = \delta_{ab}\sigma_a^2. \qquad (A16)$$

Given a rank ordering of the PC modes from smallest to largest variance, we can also construct a 3 PC filtered reconstruction of $\delta G'$ as in Ref. [23]:

$$\delta G'_{3\text{PC}}(\ln s_i) = \sum_{a=1}^{3} m_a S_{ia}, \qquad (A17)$$

and similarly use $\delta G'_{3\text{PC}}$ to construct the 3PC filtered $\Delta_{\mathcal{R}}^2$ used in the main text.

[1] C. L. Bennett, A. Banday, K. M. Gorski, G. Hinshaw, P. Jackson, P. Keegstra, A. Kogut, G. F. Smoot, D. T. Wilkinson, and E. L. Wright, Astrophys. J. **464**, L1 (1996), arXiv:astro-ph/9601067 [astro-ph].
[2] D. N. Spergel *et al.* (WMAP), Astrophys. J. Suppl. **148**, 175 (2003), arXiv:astro-ph/0302209 [astro-ph].
[3] G. Hinshaw *et al.* (WMAP), Astrophys. J. Suppl. **148**, 135 (2003), arXiv:astro-ph/0302217 [astro-ph].
[4] H. V. Peiris *et al.* (WMAP), Astrophys. J. Suppl. **148**, 213 (2003), arXiv:astro-ph/0302225 [astro-ph].
[5] M. J. Mortonson, C. Dvorkin, H. V. Peiris, and W. Hu, Phys. Rev. **D79**, 103519 (2009), arXiv:0903.4920 [astro-ph.CO].
[6] P. A. R. Ade *et al.* (Planck), Astron. Astrophys. **571**, A15 (2014), arXiv:1303.5075 [astro-ph.CO].
[7] P. A. R. Ade *et al.* (Planck), Astron. Astrophys. **571**, A16 (2014), arXiv:1303.5076 [astro-ph.CO].
[8] Y.-F. Cai, E. G. M. Ferreira, B. Hu, and J. Quintin, Phys. Rev. **D92**, 121303 (2015), arXiv:1507.05619 [astro-ph.CO].
[9] P. A. R. Ade *et al.* (Planck), Astron. Astrophys. **594**, A13 (2016), arXiv:1502.01589 [astro-ph.CO].
[10] A. G. Riess, L. Macri, S. Casertano, H. Lampeitl, H. C. Ferguson, A. V. Filippenko, S. W. Jha, W. Li, and R. Chornock, Astrophys. J. **730**, 119 (2011), arXiv:1103.2976.
[11] D. Larson, J. L. Weiland, G. Hinshaw, and C. L. Bennett, Astrophys. J. **801**, 9 (2015), arXiv:1409.7718 [astro-ph.CO].
[12] D. N. Spergel, R. Flauger, and R. Hlozek, Phys. Rev. **D91**, 023518 (2015), arXiv:1312.3313 [astro-ph.CO].
[13] G. E. Addison, Y. Huang, D. J. Watts, C. L. Bennett, M. Halpern, G. Hinshaw, and J. L. Weiland, Astrophys. J. **818**, 132 (2016), arXiv:1511.00055 [astro-ph.CO].
[14] N. Aghanim *et al.* (Planck), (2016), arXiv:1608.02487 [astro-ph.CO].
[15] A. Shafieloo and D. K. Hazra, JCAP **1704**, 012 (2017), arXiv:1610.07402 [astro-ph.CO].
[16] W. Hu and T. Okamoto, Phys. Rev. **D69**, 043004 (2004), arXiv:astro-ph/0308049 [astro-ph].
[17] S. L. Bridle, A. M. Lewis, J. Weller, and G. Efstathiou, Mon. Not. Roy. Astron. Soc. **342**, L72 (2003), arXiv:astro-ph/0302306 [astro-ph].
[18] S. M. Leach, Mon. Not. Roy. Astron. Soc. **372**, 646 (2006), arXiv:astro-ph/0506390 [astro-ph].
[19] C. Sealfon, L. Verde, and R. Jimenez, Phys. Rev. **D72**, 103520 (2005), arXiv:astro-ph/0506707 [astro-ph].
[20] C. Dvorkin, H. V. Peiris, and W. Hu, Phys. Rev. **D77**, 063008 (2008), arXiv:0711.2321 [astro-ph].
[21] H. V. Peiris and L. Verde, Phys. Rev. D **81**, 021302 (2010), arXiv:0912.0268 [astro-ph.CO].
[22] P. Paykari and A. H. Jaffe, apj **711**, 1 (2010), arXiv:0902.4399 [astro-ph.CO].
[23] C. Dvorkin and W. Hu, Phys. Rev. **D84**, 063515 (2011), arXiv:1106.4016 [astro-ph.CO].
[24] P. A. R. Ade *et al.* (Planck), Astron. Astrophys. **571**, A22 (2014), arXiv:1303.5082 [astro-ph.CO].
[25] V. Miranda, W. Hu, and C. Dvorkin, Physical Review D **91**, 063514 (2015).
[26] P. A. R. Ade *et al.* (Planck), Astron. Astrophys. **594**, A20 (2016), arXiv:1502.02114 [astro-ph.CO].
[27] J. Silk and M. S. Turner, Phys. Rev. **D35**, 419 (1987).
[28] D. Polarski and A. A. Starobinsky, Nucl. Phys. **B385**, 623 (1992).
[29] J. A. Adams, G. G. Ross, and S. Sarkar, Nucl. Phys. **B503**, 405 (1997), arXiv:hep-ph/9704286 [hep-ph].
[30] P. Hunt and S. Sarkar, Phys. Rev. **D70**, 103518 (2004), arXiv:astro-ph/0408138 [astro-ph].
[31] E. Di Valentino, A. Melchiorri, and O. Mena, Phys. Rev. **D96**, 043503 (2017), arXiv:1704.08342 [astro-ph.CO].
[32] E. Di Valentino, A. Melchiorri, E. V. Linder, and J. Silk, Phys. Rev. **D96**, 023523 (2017), arXiv:1704.00762 [astro-ph.CO].
[33] C. Dvorkin, M. Wyman, D. H. Rudd, and W. Hu, Phys. Rev. **D90**, 083503 (2014), arXiv:1403.8049 [astro-ph.CO].
[34] R. Krall, F.-Y. Cyr-Racine, and C. Dvorkin, JCAP **1709**, 003 (2017), arXiv:1705.08894 [astro-ph.CO].
[35] M. Wyman, D. H. Rudd, R. A. Vanderveld, and W. Hu, Phys. Rev. Lett. **112**, 051302 (2014), arXiv:1307.7715 [astro-ph.CO].
[36] M. Drewes *et al.*, JCAP **1701**, 025 (2017), arXiv:1602.04816 [hep-ph].
[37] N. Canac, G. Aslanyan, K. N. Abazajian, R. Easther, and L. C. Price, JCAP **1609**, 022 (2016), arXiv:1606.03057 [astro-ph.CO].
[38] L. Feng, J.-F. Zhang, and X. Zhang, Eur. Phys. J. **C77**, 418 (2017), arXiv:1703.04884 [astro-ph.CO].
[39] J. Hamann and J. Hasenkamp, JCAP **1310**, 044 (2013), arXiv:1308.3255 [astro-ph.CO].
[40] M. Costanzi, B. Sartoris, M. Viel, and S. Borgani, JCAP **1410**, 081 (2014), arXiv:1407.8338 [astro-ph.CO].
[41] P. A. R. Ade *et al.* (Planck), Astron. Astrophys. **594**, A14 (2016), arXiv:1502.01590 [astro-ph.CO].
[42] B. Hu and M. Raveri, Phys. Rev. **D91**, 123515 (2015), arXiv:1502.06599 [astro-ph.CO].
[43] S. Joudaki *et al.*, Mon. Not. Roy. Astron. Soc. **471**, 1259 (2017), arXiv:1610.04606 [astro-ph.CO].

[44] S. Peirone, M. Martinelli, M. Raveri, and A. Silvestri, Phys. Rev. **D96**, 063524 (2017), arXiv:1702.06526 [astro-ph.CO].

[45] G.-B. Zhao *et al.*, Nat. Astron. **1**, 627 (2017), arXiv:1701.08165 [astro-ph.CO].

[46] M. A. Buen-Abad, G. Marques-Tavares, and M. Schmaltz, Phys. Rev. **D92**, 023531 (2015), arXiv:1505.03542 [hep-ph].

[47] K. Enqvist, S. Nadathur, T. Sekiguchi, and T. Takahashi, JCAP **1509**, 067 (2015), arXiv:1505.05511 [astro-ph.CO].

[48] J. Lesgourgues, G. Marques-Tavares, and M. Schmaltz, JCAP **1602**, 037 (2016), arXiv:1507.04351 [astro-ph.CO].

[49] V. Poulin, P. D. Serpico, and J. Lesgourgues, JCAP **1608**, 036 (2016), arXiv:1606.02073 [astro-ph.CO].

[50] P. Ko and Y. Tang, Phys. Lett. **B762**, 462 (2016), arXiv:1608.01083 [hep-ph].

[51] P. Ko and Y. Tang, Phys. Lett. **B768**, 12 (2017), arXiv:1609.02307 [hep-ph].

[52] Z. Chacko, Y. Cui, S. Hong, T. Okui, and Y. Tsai, JHEP **12**, 108 (2016), arXiv:1609.03569 [astro-ph.CO].

[53] M. Raveri, W. Hu, T. Hoffman, and L.-T. Wang, (2017), arXiv:1709.04877 [astro-ph.CO].

[54] M. A. Buen-Abad, M. Schmaltz, J. Lesgourgues, and T. Brinckmann, (2017), arXiv:1708.09406 [astro-ph.CO].

[55] E. D. Stewart, Phys. Rev. **D65**, 103508 (2002), arXiv:astro-ph/0110322 [astro-ph].

[56] C. Dvorkin and W. Hu, Phys. Rev. **D81**, 023518 (2010), arXiv:0910.2237 [astro-ph.CO].

[57] C. Dvorkin and W. Hu, Phys. Rev. **D82**, 043513 (2010),

[58] A. Lewis and S. Bridle, Phys. Rev. **D66**, 103511 (2002), arXiv:astro-ph/0205436 [astro-ph].

[59] A. Lewis, A. Challinor, and A. Lasenby, Astrophys. J. **538**, 473 (2000), arXiv:astro-ph/9911177 [astro-ph].

[60] W. Hu and N. Sugiyama, Astrophys. J. **444**, 489 (1995), arXiv:astro-ph/9407093 [astro-ph].

[61] W. Hu and S. Dodelson, Ann. Rev. Astron. Astrophys. **40**, 171 (2002), arXiv:astro-ph/0110414 [astro-ph].

[62] S. Galli, K. Benabed, F. Bouchet, J.-F. Cardoso, F. Elsner, E. Hivon, A. Mangilli, S. Prunet, and B. Wandelt, Phys. Rev. **D90**, 063504 (2014), arXiv:1403.5271 [astro-ph.CO].

[63] W. Hu, M. Fukugita, M. Zaldarriaga, and M. Tegmark, Astrophys. J. **549**, 669 (2001), arXiv:astro-ph/0006436 [astro-ph].

[64] P. A. R. Ade *et al.* (Planck), Astron. Astrophys. **571**, A20 (2014), arXiv:1303.5080 [astro-ph.CO].

[65] S. Joudaki *et al.*, Mon. Not. Roy. Astron. Soc. **465**, 2033 (2017), arXiv:1601.05786 [astro-ph.CO].

[66] H. Hildebrandt *et al.*, Mon. Not. Roy. Astron. Soc. **465**, 1454 (2017), arXiv:1606.05338 [astro-ph.CO].

[67] M. A. Troxel *et al.* (DES), (2017), arXiv:1708.01538 [astro-ph.CO].

[68] C. H. Heinrich, V. Miranda, and W. Hu, Phys. Rev. **D95**, 023513 (2017), arXiv:1609.04788 [astro-ph.CO].

[69] W. Hu, Phys. Rev. **D84**, 027303 (2011), arXiv:1104.4500 [astro-ph.CO].

[70] H. Motohashi and W. Hu, (2017), arXiv:1704.01128 [hep-th].